

Simulations of Scalar Dispersion in Fluidized Solid–Liquid Suspensions

J. J. Derksen

School of Engineering, University of Aberdeen, Aberdeen AB24 3UE, U.K.

DOI 10.1002/aic.14372

Published online January 29, 2014 in Wiley Online Library (wileyonlinelibrary.com)

Direct, particle-resolved simulations of solid–liquid fluidization with the aim of quantifying dispersion have been performed. In addition to simulating the multiphase flow dynamics (that is dealt with by a lattice-Boltzmann method coupled to an event-driven hard-sphere algorithm), a transport equation of a passive scalar in the liquid phase has been solved by means of a finite-volume approach. The spreading of the scalar—as a consequence of the motion of the fluidized, monosized spherical particles that agitate the liquid—is quantified through dispersion coefficients. Particle self-diffusivities have also been determined. Solids volume fractions were in the range 0.2–0.5, whereas single-sphere settling Reynolds numbers varied between approximately 3 and 20. The dispersion processes are highly anisotropic with lateral spreading much slower (by one order of magnitude) than vertical spreading. Scalar dispersion coefficients are of the same order of magnitude as particle self-diffusivities. © 2014 American Institute of Chemical Engineers AIChE J, 60: 1880–1890, 2014

Keywords: computational fluid dynamics, fluidization, multiphase flow, mixing, simulation, multiscale

Introduction

Applications of liquid–solid fluidization^{1,2} include particle classification, crystal growth, leaching, heat exchange, and bioreactors for, for example, wastewater treatment. The processes carried out in liquid-fluidized beds in many cases rely on scalar (heat, species) transfer brought about and enhanced by the relative, erratic motion of solid and liquid.^{3–6} In solid–liquid scalar transfer, roughly two stages can be identified. (1) Release of the scalar in the liquid through diffusion at the solid–liquid interface. (2) Convection-dominated transport as a result of the liquid flow induced by particle motions and the pressure gradient driving the fluidization. For liquid systems that in general have high Schmidt numbers ($Sc = O(10^3)$) the first stage is confined to narrow layers around the solid particles with steep scalar gradients. This article focuses on the second stage, that is, the convection of the scalar in the interstitial liquid between the particles. Given the complexity of the liquid flow at the scale of the particles due to particle motion and the narrow, tortuous flow paths between the solids in dense suspensions, we expect the scalar spreading to depend on the (local) solids volume fraction and particle and liquid properties. The latter, we quantify by means of Reynolds numbers based on particle size and liquid–solid slip velocities.

In a previous article,⁷ an exercise similar to the one presented here was performed for granular particles. In that article, we took a small, fully periodic sample of a granular gas consisting of randomly moving and elastically colliding

monosized solid spheres that was one-way coupled to an interstitial liquid. In that case, “one-way” meant that the liquid was agitated by the moving solids, but the solids did not feel the presence of the liquid. The agitation brought about dispersion of a passive scalar contained in the liquid. This was an isotropic system that could be characterized by a dispersion coefficient that was a function of the solids volume fraction, a Reynolds number (based on the granular temperature of the solids), and the Schmidt number (the latter dependency was not investigated in Ref. 7).

Contrary to that previous article, the fluidized systems as studied in the present article are anisotropic in nature. There is an average solid–liquid slip velocity in the direction of gravity which creates anisotropic liquid flow. In addition, particle velocity fluctuations in sedimenting (and therefore also in fluidized) systems are known to be anisotropic with stronger fluctuations in the vertical direction compared to the horizontal directions.^{8–10} Anisotropy of particle motion will certainly reflect in scalar spreading. Finally, relative particle locations are not fully random in fluidization as can be witnessed from radial and angular distribution functions.^{11,12} We therefore expect the dispersion of a scalar dissolved in the liquid in fluidized systems to be the result of an intricate interplay between the erratic (however, not fully random) motion of the solid particles and the (related) flow of interstitial liquid that has an average, as well as a fluctuating component. The practical relevance of mass transfer in liquid–solid fluidized systems and their complex, anisotropy characteristics warrant a study of scalar spreading in liquid-fluidized beds.

The literature on sedimentation is relevant to the current research, since sedimentation and fluidization are governed by the same (hindered settling) dynamics. The recent review

Correspondence concerning this article should be addressed to J.J. Derksen at jderksen@abdn.ac.uk.

by Guazzelli and Hinch⁸ summarizes current understanding of sedimentation and hints at outstanding issues and challenges. Important topics—specifically, as here we study scalar dispersion in the continuous phase, a process brought about by random particle motion—are particle velocity fluctuations and hydrodynamic (or self) diffusion of particles and their dependency on solids volume fraction, Reynolds number, and domain size.^{11,13–17} Self-diffusion can be thought of as the particle counterpart of scalar dispersion in the liquid phase. So far, research on particle fluctuations and self-diffusivity has mostly (not exclusively) considered low particle Reynolds numbers ($Re \ll 1$) in fairly dilute systems; typically $\phi \approx 0.1$ and ϕ hardly exceeding 0.4.

The aim of the current study is to quantify scalar spreading in liquid–solid fluidization over a range of solids volume fractions and Reynolds numbers. Trends in scalar dispersion are compared to those in particle self-diffusion. With a view to the applications we are interested in, we focus on moderately dense to dense suspensions ($0.2 \leq \phi \leq 0.5$) and “inertial” particles with single-particle settling Reynolds numbers Re_∞ of order 10. The situations considered in this article are typical for processes that involve particles with sizes of the order of 0.1–0.5 mm in watery liquids that are applied for leaching and electrolytic recovery of metals.²

The research described here is purely computational. It considers monosized, solid spheres (radius a , density ρ_p) immersed in Newtonian liquid (kinematic viscosity ν and density ρ). The three-dimensional (3-D) rectangular domain is fully periodic and contains of the order of a thousand particles. The hydrodynamics can be largely captured by two input parameters: the solids volume fraction ϕ and the single-particle settling Reynolds number $Re_\infty \equiv 2aU_\infty/\nu$. In the simulations, we resolve the solid–liquid interfaces. A lattice-Boltzmann (LB) method^{18,19} simulates the flow of interstitial liquid. It is coupled to an immersed boundary method that imposes no-slip at the surfaces of the particles. The immersed boundary method provides the hydrodynamic forces and torques that—in addition to net gravity—drive linear and angular motion of the particles. Particle motion is then coupled back to liquid flow through the no-slip condition. The typical resolution is such that the sphere radius a spans six units of the uniform, cubic lattice. The spherical particles collide according to a hard-sphere algorithm. For estimating scalar spreading, a convection–diffusion equation is solved by means of a finite-volume method for a scalar with concentration c dissolved in the liquid. Solid–liquid mass transfer is not considered. In a scalar transport sense, the particles are inert. A zero normal gradient condition ($\partial c/\partial n=0$) applies at their surface.

A limitation of the current study is the size of the computational domain. The resolution demanded for the hydrodynamic and scalar fields, the denseness of the suspension (solids volume fraction up to 0.5), and computational restraints do not allow for domains for which particle self-diffusivity is expected to be independent of domain size.¹⁴ The domains used in this study are larger (generally by a factor of two) in vertical direction compared to the horizontal directions to somewhat mitigate size effects.¹³

Eventually, the results of the particle-resolved simulations as presented here could find their way into less resolved simulations capturing larger (equipment size) scales such as Euler–Euler type simulations,²⁰ or discrete element method simulations with unresolved particles.²¹ In a multiple-scales

approach, the dispersion coefficients as estimated in the present article then would serve as effective diffusion coefficients to calculate large-scale mixing, including local effects by considering the way the scalar dispersion process depends on local volume fractions and slip velocities.

This article is organized along the following lines: first, the flow system is defined by means of a set of dimensionless numbers. In the next section, the simulation routines are discussed: multiphase flow dynamics with resolved particles, scalar transport, and also data analyses to determine scalar dispersion coefficients and particle self-diffusivities. In the Results section, first, the solid–liquid system is shown to demonstrate the proper hindered settling behavior as described by average velocities. Then scalar spreading is discussed and scalar dispersion is compared to particle self-diffusivity.

Flow System

We consider fully periodic, 3-D domains that contain incompressible Newtonian fluid with density ρ and kinematic viscosity ν , and uniformly sized solid spherical particles with radius a and density ρ_p . The domain size is W in the two horizontal directions, and $2W$ in the vertical (x) direction. The solids volume fraction ϕ is in the range 0.20–0.50; the aspect ratio W/a has been fixed to 24 (except for simulations that assess domain size effects). The solid over liquid density ratio ρ_p/ρ is 4.0. Each solid sphere experiences a net gravity force $\mathbf{F}_g = -(\rho_p - \bar{\rho}) \frac{4}{3} \pi a^3 g \mathbf{e}_x$, with $\bar{\rho} = \phi \rho_p + (1 - \phi) \rho$ the mixture density and g gravitational acceleration. In order to balance forces over the periodic domain we apply a uniform body force acting in the positive x -direction on the liquid $\mathbf{f} = (\bar{\rho} - \rho) g \mathbf{e}_x$.²²

The two main independent input variables in this study are the solids volume fraction ϕ and the single-particle settling Reynolds number $Re_\infty = U_\infty 2a/\nu$, where U_∞ is determined by a force balance over a sphere. In this force balance, the drag force correlation due to Schiller and Naumann²³ has been used: $C_D = 24(1 + 0.15 Re_\infty^{0.687})/Re_\infty$. The range of Re_∞ was 3.37–17.4. The way scalar dispersion in the liquid and self-diffusivity of particles depend on ϕ and Re_∞ is the main outcome of this research.

The concentration c of the scalar dissolved in the liquid phase satisfies a convection–diffusion equation

$$\frac{\partial c}{\partial t} + \mathbf{u} \cdot \nabla c = \Gamma \nabla^2 c \quad (1)$$

with \mathbf{u} the liquid velocity field and Γ the diffusion coefficient. The Schmidt number is defined as $Sc \equiv \nu/\Gamma$. We set $Sc = 1000$. The numerical implications of this high value will be discussed in the next section. Periodic conditions apply to the scalar on the planes bounding the simulation domain. At the sphere surfaces $\partial c/\partial n = 0$ applies, with n the direction normal to the solid surface. The scalar is passive; its concentration field does in no way affect the flow dynamics.

Modeling Approach

Multiphase flow simulation

We used the LB method^{18,19} to solve the flow of liquid in between the spheres. The method has a uniform, cubic grid (grid spacing Δ). The specific scheme used here is due to Somers.²⁴ The no-slip condition at the spheres’ surfaces was

dealt with by means of an immersed boundary (or forcing) method.^{25,26} In this method, the sphere surface is defined as a set of closely spaced points (the typical spacing between points is 0.7Δ), not coinciding with lattice points. At these points, the (interpolated) fluid velocity is forced to the local velocity of the solid surface according to a control algorithm. The local solid surface velocity has contributions from translational and rotational motion of the sphere under consideration. Adding up (discrete integration) per spherical particle, the forces needed to maintain no-slip provides us with the force the fluid exerts on the spherical particle. Similarly the hydrodynamic torque exerted on the particles can be determined. Forces and torques are subsequently used to update the linear and rotational equations of motion of each spherical particle.²²

It should be noted that having a spherical particle on a cubic grid requires a calibration step, as earlier realized by Ladd.²⁷ He introduced the concept of a hydrodynamic radius. The calibration involves placing a sphere with a given radius a_g in a fully periodic cubic domain in creeping flow and (computationally) measuring its drag force. The hydrodynamic radius a of that sphere is the radius for which the measured drag force corresponds to the expression for the drag force on a simple cubic array of spheres due to Sangani and Acrivos,²⁸ which is an extension toward higher solids volume fractions of the analytical expression of Hasimoto.²⁹ Usually a is slightly larger than a_g with $a - a_g$ typically equal to half a lattice spacing or less. The simulations presented in this article have a resolution such that $a = 6\Delta$. Earlier simulations of liquid–solid fluidization at comparable solids volume fractions and Reynolds numbers,²² and simulations assessing drag in static sphere assemblies³⁰ have demonstrated that simulations with a resolution of $a = 6\Delta$ are consistent to those on finer grids (up to $a = 16\Delta$).

Once the spatial resolution is fixed, the temporal resolution of the LB simulations goes via the choice of the kinematic viscosity ν . The kinematic viscosity was set to 0.02 in lattice units (space unit is Δ , time unit is one time step Δt) so that for the default resolution the viscous time scale $\frac{a^2}{\nu}$ corresponds to $1800\Delta t$. The convective time scale $\frac{a}{U_\infty}$ is in the range $200\text{--}1900\Delta t$. Combined with $a = 6\Delta$, the latter implies that particles move only over a small fraction of Δ during one time step.

Fixed-grid simulations involving moderately dense suspensions as discussed here require explicit inclusion of subgrid lubrication forces³¹ to account for very short range interaction between particles that cannot be resolved by the computational grid and thus occur at distances of particle surfaces less than approximately one lattice spacing. A procedure for including lubrication forces has been proposed and tested in earlier articles.²² Only radial lubrication forces were considered in the simulations. The lubrication force model has two parameters. The first is the distance s_0 between two sphere surfaces below which the lubrication force becomes active. It has been set to $s_0 = 0.2a$. In the default case of $a = 6\Delta$, $s_0 = 1.2\Delta$. The second parameter relates to surface roughness. The radial lubrication force is inversely proportional to the distance s between surfaces and thus diverges for $s \rightarrow 0$. However, once s approaches the surface roughness of the particles, the $1/s$ behavior of the lubrication force is expected no longer to be valid. In the simulations, this has been accounted for by saturating the lubrication force once two surfaces have a distance less than s_1 . The parameter s_1

has been set to $s_1 = 2 \times 10^{-3}a$ and can be interpreted as a surface roughness length scale.

Lubrication generally is not strong enough to prevent collisions between spheres. Upon solid–solid contact, two spheres undergo a hard-sphere collision according to the two-parameter model of Yamamoto et al.³² The restitution coefficient and friction coefficient were set to $e = 1$ and $\mu_f = 0$, respectively, throughout this work. The hard-sphere algorithm is event driven: within an LB time step Δt , the particles move with constant velocity until a collision between two particles is detected. At that moment all particles are frozen, the binary collision is carried out (which means an update of the linear velocities of the two particles involved in the collision; as $\mu_f = 0$, angular velocities do not change upon collision), and the particles continue moving until the next collision or the end of Δt , whichever comes first.

Scalar transport

The convection–diffusion equation in the scalar concentration c (Eq. 1) has been solved with an explicit finite-volume scheme on the same grid as used by the LB method. To limit numerical diffusion, we apply TVD (Total Variation Diminishing) discretization with the Superbee flux limiter for the convective fluxes.^{33,34} We step in time according to an Euler explicit scheme. We do not allow scalar concentration inside the spherical particles. At the surface of the particles, we impose the $\frac{\partial c}{\partial n} = 0$ condition by means of a ghost-cell technique³⁵ that involves interpolation of scalar concentrations. The $\frac{\partial c}{\partial n} = 0$ condition is also used for assigning concentrations to grid nodes that get uncovered by a moving solid particle. As particles typically move less than 0.025Δ per time step, an uncovered node is always close to a solid–liquid interface. We draw the normal out of the particle into the fluid at the position of the uncovered node. By interpolation, we determine the concentration on the normal one additional grid spacing into the fluid and assign that concentration to the uncovered node. Given the denseness of the suspension this cannot always be done; it regularly occurs that a grid cell gets uncovered in between two closely spaced particles, for example, moving away from each other after a collision. The outward normal from one particle then penetrates the other particle so that no concentration data is available. In such cases, we assign the average concentration in the direct vicinity to the uncovered grid node, whereas keeping that vicinity as small as possible. Particles covering and uncovering grid nodes containing scalar makes the simulations not inherently mass conservative; the severity of this issue has been assessed in the Results section.

As stated above, in the computer code the Schmidt number was set to $Sc = 1000$ which means that diffusive scalar transport length scales would be approximately $\sqrt{Sc} \approx 30$ times smaller than hydrodynamic scales. As the scalar grid has the same resolution as the hydrodynamic (LB) grid, the scalar field is likely under-resolved and we should not have the illusion that we simulate a system with $Sc = 1000$. We do, however, determine a high-Schmidt number scalar field, that is, a field dominated by convection rather than diffusion. This notion is based on experience described in our previous article,⁷ on mixing by granular particles where it was shown that grid refinement by a linear factor of two did not change (within 3%) scalar spreading as quantified by the width of a scalar distribution. If under-resolution and (related) numerical diffusion would have had

strong impact on scalar transport, it should have appeared as a much larger change of scalar spreading upon grid refinement.

Scalar data analysis

The two main interests in this article are scalar dispersion and particle self-diffusion in liquid-fluidized beds, and how much different these processes are in the vertical and horizontal directions. Regarding scalar dispersion, we set up the simulations such that they can be analyzed in one-dimensional (1-D) manners (as we also did in Ref. 7). Simulations are started from a random particle configuration, and zero liquid and solid velocity. We switch on gravity and the balancing body force on the liquid (see the Flow System section) and monitor the development toward dynamically steady flow. After this stage is reached, the scalar is introduced in horizontal and vertical slabs with thickness $2a$: In the liquid, in the slab $c = 1$ and outside the slab $c = 0$. The simulations are continued, now including solving scalar transport equations in addition to the multiphase flow dynamics.

Data reduction is achieved by contracting the 3-D, time dependent concentration fields to 1-D, time dependent concentration distributions by averaging over the homogeneous directions. For the vertical (x) direction: $\tilde{c}_{\text{vert}}(x, t) \equiv \frac{1}{W^2} \int_0^W \int_0^W c_{\text{vert}}(x, y, z, t) dy dz$; for a horizontal (e.g., y) direction: $\tilde{c}_{y,\text{hor}}(y, t) \equiv \frac{1}{W^2} \int_0^W \int_0^W c_{y,\text{hor}}(x, y, z, t) dx dz$.

We solve multiple (eight in total) concentration fields per flow simulation. Each concentration field has its own initial scalar condition (four equally spaced horizontal slabs, four vertical slabs with two having x and z and two having x and y as homogeneous directions). The various scalar realizations we shift and subsequently average to limit noise. Noise is the result of the erratic nature of the particle motion and thus the scalar spreading process. The averaged, 1-D concentration profiles are fitted to parameterized distributions (normal distributions for horizontal spreading; skewed normal distributions for vertical spreading). The evolution of the fitting parameters with time is used to quantify the spreading process and eventually determine dispersion coefficients. The fitting procedure is explained in more detail when discussing the simulation results.

Particle self-diffusivity

Particle self-diffusion coefficients have been determined through monitoring over time the mean-square displacement of the particles due to fluctuating motion in the three coordinate directions

$$\begin{aligned} \langle \Delta x_p^2 \rangle(t) &= \langle [x_p(t+\tau) - x_p(\tau)]^2 \rangle - \langle x_p(t+\tau) - x_p(\tau) \rangle^2 \\ \langle \Delta y_p^2 \rangle(t) &= \langle [y_p(t+\tau) - y_p(\tau)]^2 \rangle \\ \langle \Delta z_p^2 \rangle(t) &= \langle [z_p(t+\tau) - z_p(\tau)]^2 \rangle \end{aligned} \quad (2)$$

The $\langle \rangle$ brackets stand for ensemble averaging, which in the practice of our simulations means that we evaluate the time series in Eq. 2 for each particle and then average over all particles. A correction for the average motion is only necessary in the vertical (x) direction. If particle motion is a diffusive process, mean-square displacements are linear in time

$$\langle \Delta x_p^2 \rangle(t) = 2D_{p,\text{vert}} t, \quad \langle \Delta y_p^2 \rangle(t) = 2D_{p,\text{hor}} t, \quad \langle \Delta z_p^2 \rangle(t) = 2D_{p,\text{hor}} t \quad (3)$$

with $D_{p,\text{vert}}$ and $D_{p,\text{hor}}$ self-diffusion coefficients in vertical and horizontal direction, respectively. Further details, specifi-

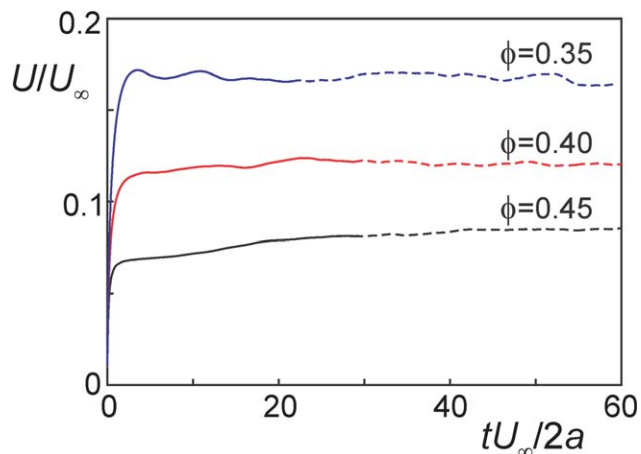


Figure 1. Time series of the volume-average superficial slip velocity U .

Startup from zero particle and liquid velocity. Overall solids volume fraction as indicated. During the dashed parts of the curves (and beyond) scalar transport was simulated in conjunction with multiphase flow. $Re_\infty = 10$. [Color figure can be viewed in the online issue, which is available at wileyonlinelibrary.com.]

cally regarding the fitting procedure to determine $D_{p,\text{vert}}$ and $D_{p,\text{hor}}$ from Eq. 3 are provided in the section *Self-diffusion of particles and relation to scalar spreading*.

Results

Hindered settling

The simulations are started from a random assembly of monosized, spherical solid particles in liquid in a fully periodic domain with solids and liquid having zero velocity.

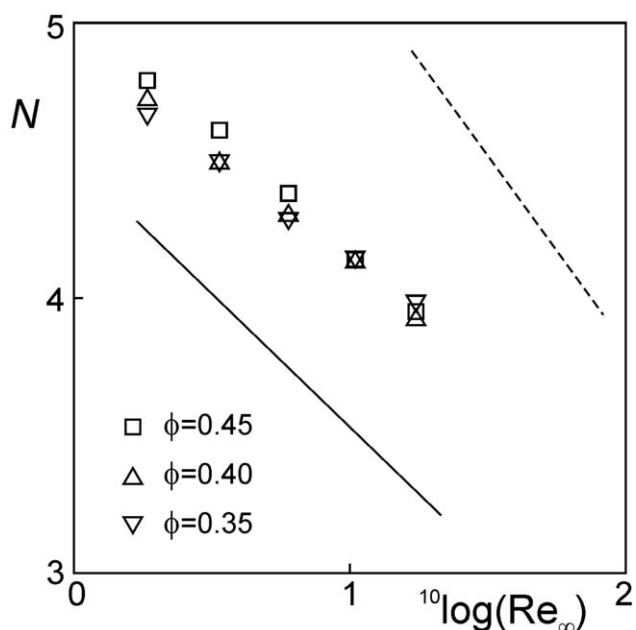


Figure 2. The Richardson and Zaki exponent N as a function of Re_∞ for various values of the solids volume fraction ϕ .

The lines represent dependencies of N on Re_∞ due to Richardson and Zaki³⁶ (solid line) and Di Felice³⁷ (dashed line).

This system is developed to a dynamic steady state. To monitor this development, the volume-average superficial slip velocity U between liquid and particles: $U \equiv (1-\phi) [\langle u \rangle - \langle u_p \rangle]$ is followed in time, see Figure 1. In the expression for U , $\langle u \rangle$ is the velocity in x -direction averaged over the liquid volume and $\langle u_p \rangle$ the x -velocity averaged over the particle volume. Figure 1 shows that after a time period of $tU_\infty/2a=20-30$, a steady state is reached. The figure also shows the effect of hindrance as U decreases for increasing ϕ at constant Re_∞ . The velocity scale U can be interpreted as the particle settling speed as would be observed in a stationary reference frame (as in a settling experiment). In a settling experiment, solids volume moving down is compensated for by liquid volume moving up: $\langle u_p \rangle \phi + \langle u \rangle (1-\phi) = 0$;

this implies that $U \equiv -\langle u_p \rangle$. If hindered settling is described with a Richardson and Zaki (RZ) correlation^{36,37} $U/U_\infty = (1-\phi)^N$, the time-averaged simulated values of U can be used to estimate the exponent N . We do so in Figure 2. The figure shows that the RZ correlation adequately captures the solids volume fraction dependency of U : the values of N only weakly depend on ϕ . Furthermore, values for N and its dependency on Re_∞ are in reasonable agreement with experimental data, as can be seen from the empirical correlations^{36,37} included in Figure 2. The size of the simulation domain has negligible influence on the results as presented in Figure 2. The case with $\phi=0.40$ and $Re_\infty = 10.4$ that shows $N=4.11$ in Figure 2 has been repeated for a taller domain (domain height $72a$ instead of the default $48a$)

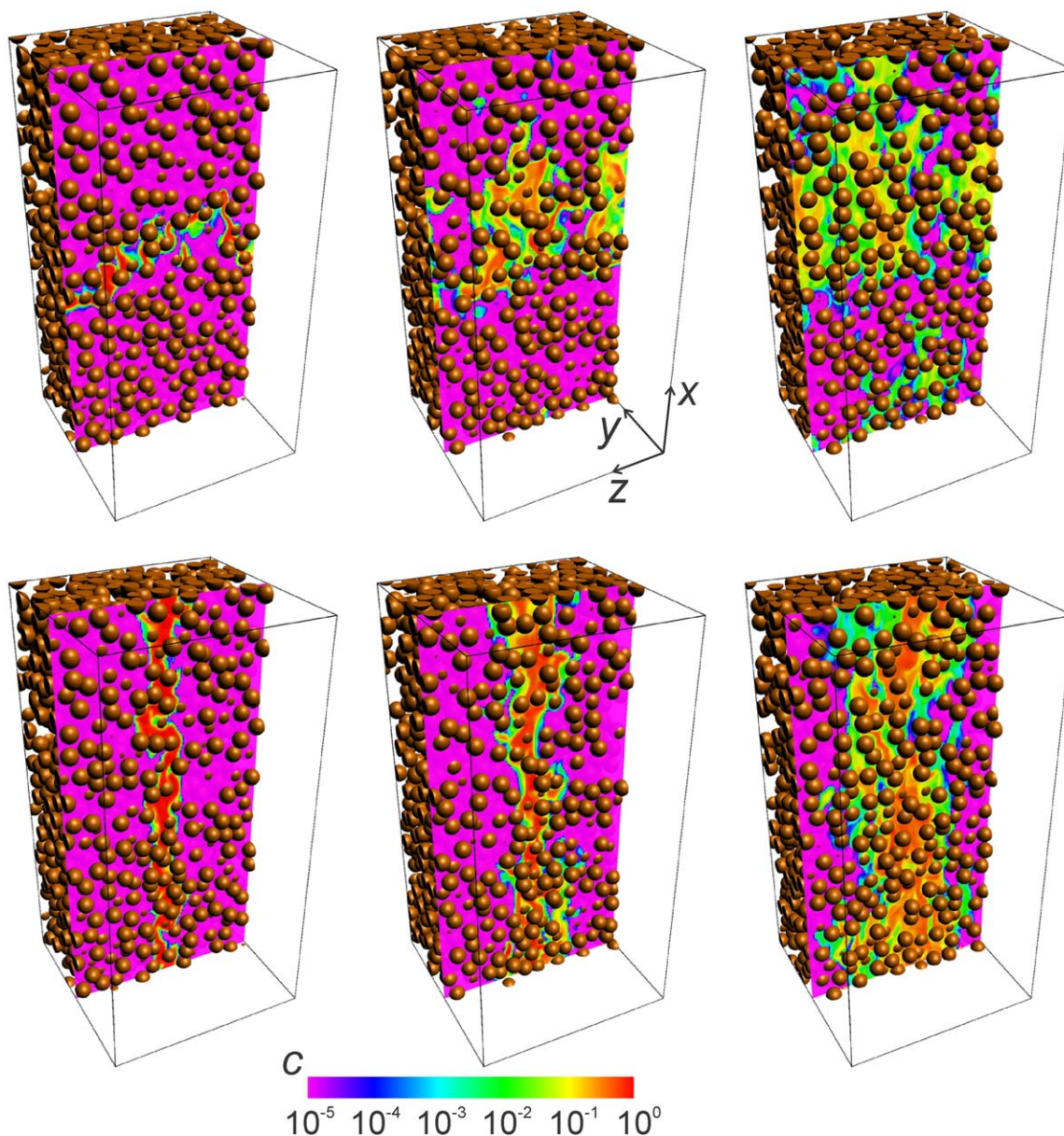


Figure 3. Impressions of scalar spreading in the plane $y=W/2$ for the flow case with $\phi=0.40$ and $Re_\infty=10$ (base-case).

Upper row: scalar that initially formed a horizontal slab halfway the domain; bottom row: vertical scalar slab. From left to right: different moments in time; $\frac{tU}{2a(1-\phi)} = 1, 3, \text{ and } 6$, respectively. Only spheres with center location $y_p \geq W/2 - a$ are shown. Note the logarithmic color scale. [Color figure can be viewed in the online issue, which is available at wileyonlinelibrary.com.]

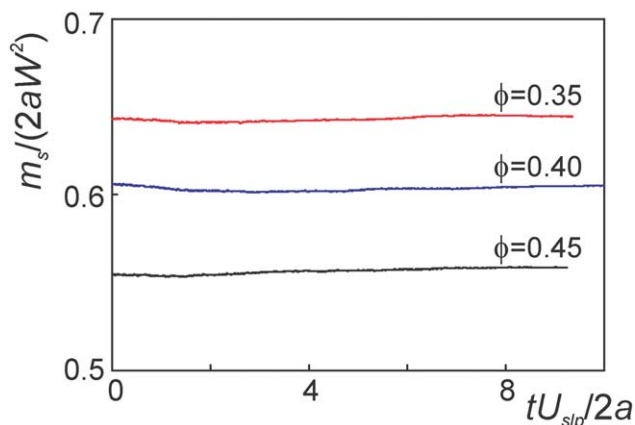


Figure 4. Scalar mass as a function of time for three cases with $Re_\infty=10.4$.

The scaling of scalar mass is such that $\frac{m_s}{2aW^2} \approx 1-\phi$. [Color figure can be viewed in the online issue, which is available at wileyonlinelibrary.com.]

and for a wider domain (width in both horizontal directions $36a$ instead of the default $24a$) leading to $N=4.10$ and $N=4.09$, respectively.

Scalar spreading

After the liquid–solid system has reached a dynamic steady state, scalar concentrations are introduced in the simulations. Impressions of the scalar spreading as a result of the motion of liquid and solid are presented in Figure 3. The simulation shown in Figure 3 will be referred to as the base-case. The two main variables in this work are ϕ and Re_∞ ; the base-case has $\phi=0.40$ and $Re_\infty=10.4$ and further the default settings as described above. The time instants in Figure 3 have been made dimensionless with the average slip velocity $U_{slip} \equiv \langle u \rangle - \langle u_p \rangle = U/(1-\phi)$. In the top row, we see how the scalar that is initially confined to a horizontal layer (slab) with a thickness equal to the sphere diameter gets dispersed. On average, the scalar is convected up as there is an average liquid flow in the positive x -direction. We also

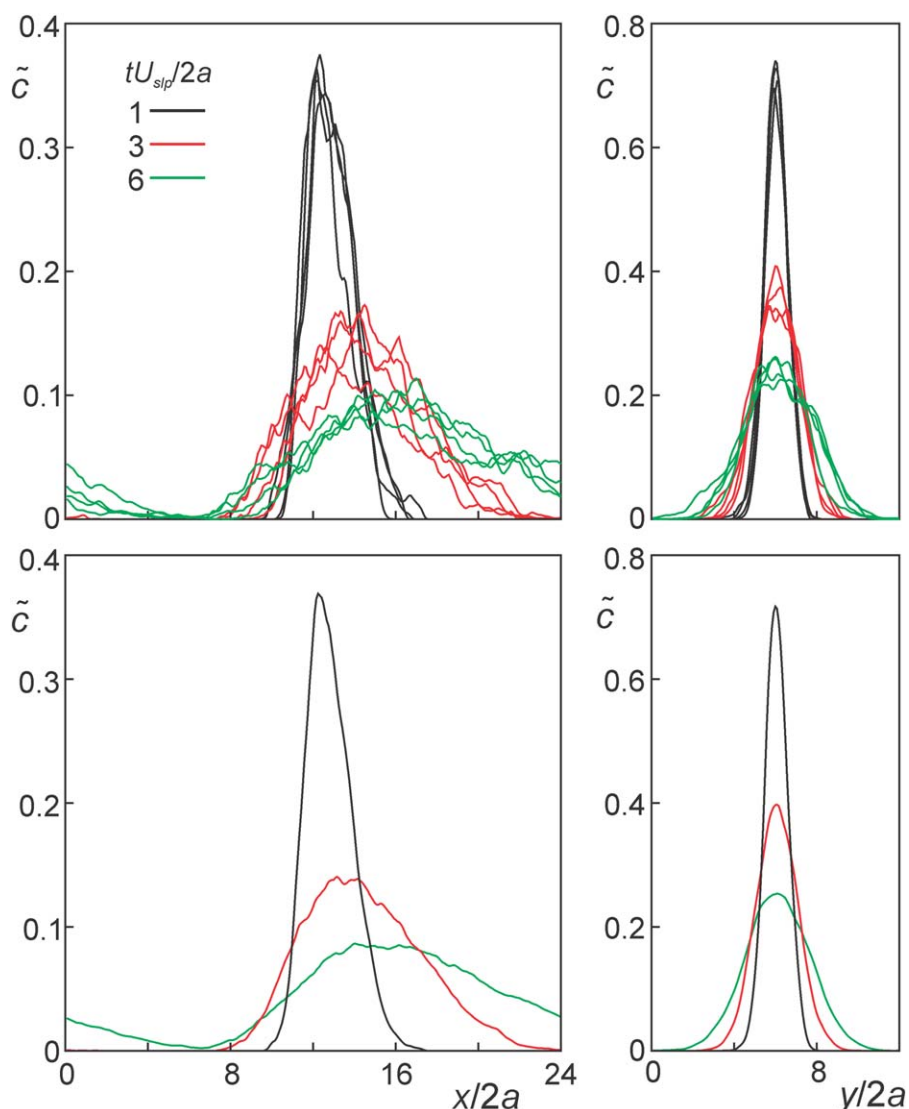


Figure 5. 1-D concentration profiles for the base-case at three moments in time as indicated.

Left: vertical scalar spreading; right: horizontal spreading. Top: profiles based on individual scalar fields (with different initial slab locations); bottom: averages over 12 individual scalar fields. [Color figure can be viewed in the online issue, which is available at wileyonlinelibrary.com.]

observe that the scalar spreads asymmetrically: the concentration gradients at the lower end of the scalar layer are steeper compared to the upper end. The right panel of the top row illustrates the periodic conditions: scalar that has left through the top boundary re-enters through the lower boundary. The bottom row of Figure 3 is based on the same liquid–solid simulation (this can be judged by comparing sphere locations). It shows the spreading of a scalar that was initially confined to a vertical slab of thickness $2a$ in the middle of the domain. The width of this scalar layer increases at a clearly slower pace compared to the horizontal layer, indicating anisotropic dispersion.

Figure 4 shows time series of the total scalar mass as a function of time. As the moving spheres cover and uncover nodes that contain scalar, and as the cover and uncover processes are not directly related, scalar mass is not inherently conserved and Figure 4 shows weak short-time and longer-time fluctuations. Overall mass varies by less than 1% over a time range of $\frac{tU_{slp}}{2a} = O(10)$.

Sample 1-D concentration profiles (concentration fields averaged over homogeneous directions) are shown in Figure 5. The individual 1-D profiles confirm the qualitative observations made above: upward convection and asymmetric distributions for horizontal scalar layers spreading in vertical direction; narrower (and symmetric) distributions for vertical layers that spread horizontally. The scatter in the individual 1-D profiles hinders further analysis of the scalar dispersion process. For this reason, we generate multiple 1-D profiles under the same physical conditions and average them. In the first place, each simulation has multiple, independent scalar layers (four horizontal, four vertical). The spacing between

the layers is $W/2=12a$ so that the local particle assemblies that are responsible for the spreading process can be considered statistically independent. In the second place, we repeat the simulations a few times, starting from different (fully developed) initial liquid–solid flow conditions. In the bottom part of Figure 5, the profiles are the average of 12 realizations (three simulations with four scalar fields per simulation). Further analysis will be based on these average, 1-D distributions, and the way they develop in time. Our main interest is in the variance of the distributions to quantify scalar spreading.

We have tried to determine variance and also skewness of concentration distributions in various ways and have eventually settled on a procedure based on curve fitting. It has the advantage of taking into account the periodicity of the simulation domain. Given computational limitations on the size of the flow domains, periodic copies of scalar distributions start to interfere at fairly early stages of the spreading process; that is, the head of one distribution quickly overlaps with the tail of the next. Directly integrating the discrete data constituting distribution functions to determine their moments introduces two errors: overlap of subsequent distributions, and clipping of distributions to the length or width of the domain. The alternative is fitting the distributions to assumed functions for which we use analytical expressions and then calculating the moments of the fitted functions. By fitting to periodic repetitions of the analytical functions, rather than to a single function, the periodicity of the simulations is directly accounted for.

Given the symmetry in horizontal directions, a natural choice for the horizontal distribution function is the normal distribution with variance σ^2 and average μ

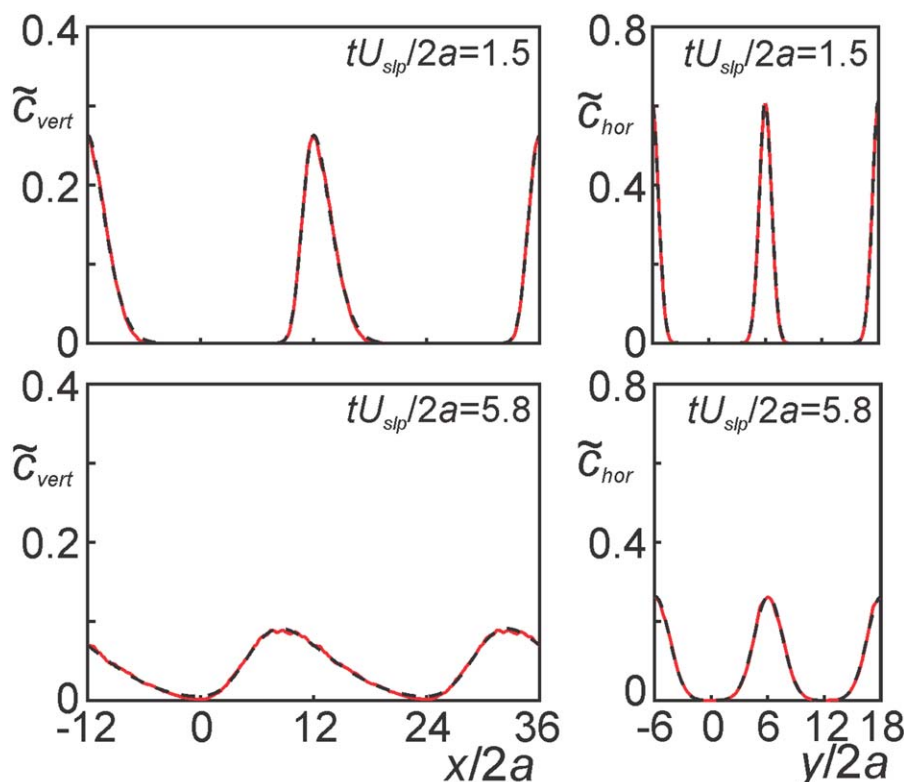


Figure 6. Average concentration profiles (red curves) at different moments in time, and their fits (black dashed curves).

Base-case conditions. [Color figure can be viewed in the online issue, which is available at wileyonlinelibrary.com.]

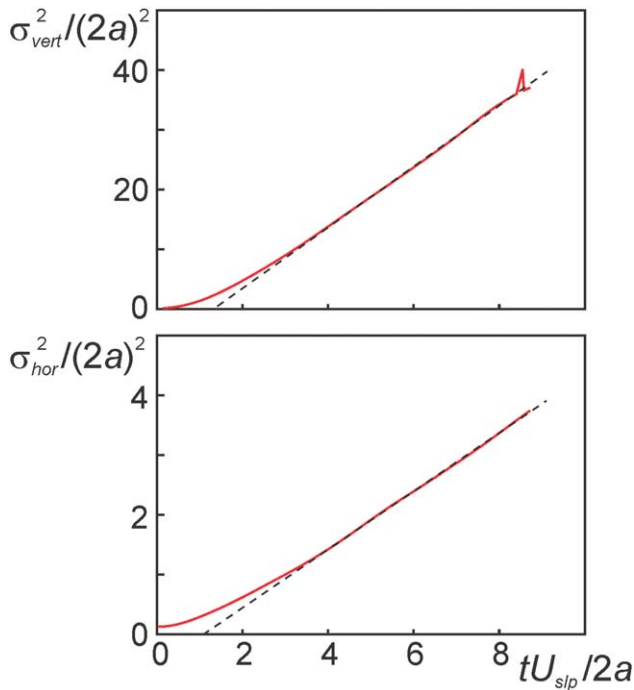


Figure 7. Red curves: time series of the variance of the concentration profile in vertical direction (σ_{vert}^2) and horizontal direction (σ_{hor}^2).

The dashed lines are best fits of the approximately linear portions of the red curves. Base-case conditions. [Color figure can be viewed in the online issue, which is available at wileyonlinelibrary.com.]

$$\hat{c}_{y,hor}(y, t) = \frac{1}{\sigma(t)\sqrt{2\pi}} \exp\left[-\frac{(y-\mu)^2}{2\sigma^2(t)}\right] \quad (4)$$

The superscript \wedge indicates a fitting function. Simulated horizontal profiles are shifted such that $\mu=W/2$ and μ is not a degree of freedom in the fitting process, only σ is. The vertical concentration distributions are clearly nonsymmetric, see Figure 5, left panels. These are fitted to a skewed normal distribution³⁸ defined as

$$\hat{c}_{vert}(x, t) = \frac{1}{\omega(t)\sqrt{2\pi}} \left[1 + \operatorname{erf}\left(\frac{\alpha(t)(x-\xi)}{\omega(t)\sqrt{2}}\right) \right] \exp\left[-\frac{(x-\xi)^2}{2\omega^2(t)}\right] \quad (5)$$

with now three fitting parameters: ξ , $\omega(t)$, and $\alpha(t)$. The parameter ξ controls the (arbitrary) location of the distribution along the (vertical) x -axis. Our main interest is in how ω and α evolve in time since they determine variance σ^2 and also skewness γ

$$\sigma^2 = \omega^2 \left(1 - \frac{2}{\pi} \frac{\alpha^2}{1 + \alpha^2} \right) \quad (6)$$

$$\gamma = \frac{4 - \pi}{2} \frac{(\delta\sqrt{2/\pi})^3}{(1 - 2\delta^2/\pi)^{3/2}} \quad \text{with } \delta \equiv \frac{\alpha}{\sqrt{1 + \alpha^2}}$$

The choice for a skewed normal distribution is a purely heuristic one and is justified by an apparent match between simulation data and the fitting function. As noted above, rather than fitting a single function, we fit periodic repetitions of Eqs. 4 and 5 that are shifted by $y = \pm W$ for Eq. 4 and $x = \pm 2W$ for Eq. 5. Sample fitting results are given in Figure 6 for vertical, as well as for horizontal concentration distributions related to the base-case.

The manner in which σ_{vert}^2 increases with time as given in the top panel of Figure 7 is typical. There is an initial non-linear stage due to the top-hat (i.e., non-Gaussian) initial concentration profile. Then there is a linear portion, and finally the curve levels off and sometimes starts showing erratic scatter (as the spike in Figure 7). The leveling off (and scatter) is the result of interference between periodic copies, combined with a weak signal compared to the inherent noise in the concentration distributions at later stages. Time series of σ_{hor}^2 (bottom panel of Figure 7) behave similarly at the start but stay linear for a longer period of time. Clearly the horizontal spreading is slower and thus less plagued by the issues that make σ_{vert}^2 level off at later times.

We usually are able to identify a time window after start-up and before leveling over which σ_{vert}^2 increases linearly

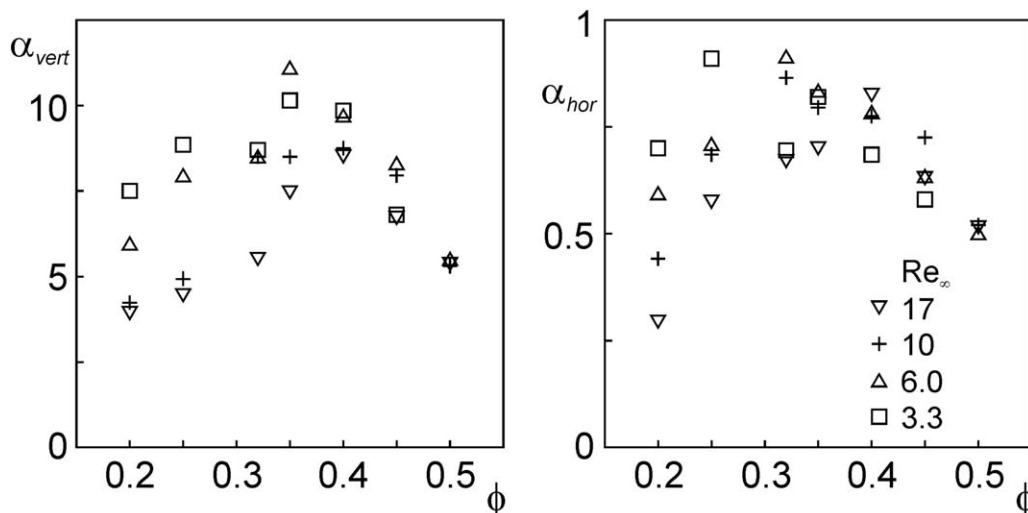


Figure 8. Dimensionless scalar dispersion coefficients in vertical (α_{vert} left) and horizontal direction (α_{hor} right) as a function of solids volume fraction ϕ for four different Re_∞ as indicated.

Error estimates: $\pm 20\%$ for α_{vert} ; $\pm 10\%$ for α_{hor} .

and we base the scaled scalar dispersion coefficient on fitting these portions with straight lines: $\frac{\sigma_{vert}^2}{(2a)^2} = K_{vert} \frac{U_{slp}}{2a} t + offset$. As diffusion/dispersion processes behave as $\sigma^2 = 2Dt$, the fitting parameter $K_{vert} = \frac{D_{p,vert}}{aU_{slp}}$ is a nondimensional dispersion coefficient in which the index *vert* denotes vertical dispersion. However, to conform with the experimental literature¹⁰ on particle self-diffusivity where diffusivity is scaled with velocity U instead of U_{slp} , our results on scalar dispersion will be presented as $\alpha_{vert} = \frac{K_{vert}}{(1-\phi)} = \frac{D_{p,vert}}{aU}$. The same fitting procedure is used to find the scaled horizontal scalar dispersion coefficient α_{hor} . Based on reproducibility tests, we estimate the uncertainty for α_{vert} as $\pm 20\%$. The reproducibility of α_{hor} is significantly better: it has an estimated error of $\pm 10\%$. The difference in errors is mainly due to the linearity of σ^2 extending over longer time for horizontal spreading.

Results of the scalar dispersion coefficients in vertical and horizontal direction as a function of solids volume fraction for four values of Re_∞ are given in Figure 8. Dispersion coefficients in the horizontal direction are one order of magnitude lower than in vertical direction. The trends in horizontal and vertical spreading with respect to ϕ and Re_∞ are, however, the same. At the high end of solids volume fractions, α_{vert} and α_{hor} are largely independent of Re_∞ , and are at the relatively low values of 5 and 0.5, respectively. Upon decreasing ϕ , the dimensionless dispersion coefficients increase. They do so in ways that depend on the Reynolds number, the increase being stronger for the lower Re_∞ . In the range $0.25 \leq \phi \leq 0.35$ vertical and horizontal dispersion coefficients reach maximum values. The decrease of α_{vert} and α_{hor} that occur when ϕ is lowered further again depends on Re_∞ , with hardly any decrease for $Re_\infty = 3.3$ (the lowest Re_∞) and strong decrease for $Re_\infty = 17$ (the highest Re_∞).

For interpretation of these results, first the results on self-diffusivity of particles are discussed.

Self-diffusion of particles and relation to scalar spreading

Examples of ensemble-averaged mean-square displacement of particles as a function of time in vertical (x) and horizontal (y) direction are given in Figure 9. After a start-up phase, the time series show approximately linear behavior. We note that the experimental time series presented in Ref. 10 look very similar, including the nonlinearity for short times (Figure 9 in Ref. 10), as what is shown in Figure 9 (in the current article). As expected, vertical mean-square displacement is stronger (by almost an order of magnitude) than horizontal mean-square displacement. To determine self-diffusion coefficients, the straight parts of the time series have been fitted with linear function, the slopes of which are the self-diffusion coefficients. The scaling of self-diffusion coefficients with particle radius and average particle settling velocity as applied here is in accordance with Ref. 10; the nondimensional self-diffusion coefficients in vertical and horizontal direction are recognized as $\beta_{vert} = \frac{D_{p,vert}}{aU}$ and $\beta_{hor} = \frac{D_{p,hor}}{aU}$, respectively. Linearities of mean-square displacement with time generally span a significant time window leading to relatively low uncertainties in β_{vert} and β_{hor} . They are estimated as $\pm 10\%$ based on reproducibility tests.

In Figure 10, it is shown how self-diffusivity depends on the solids volume fraction for four different Reynolds numbers. The first, important observation is that self-diffusivity and scalar dispersion coefficients (see Figure 8) have the

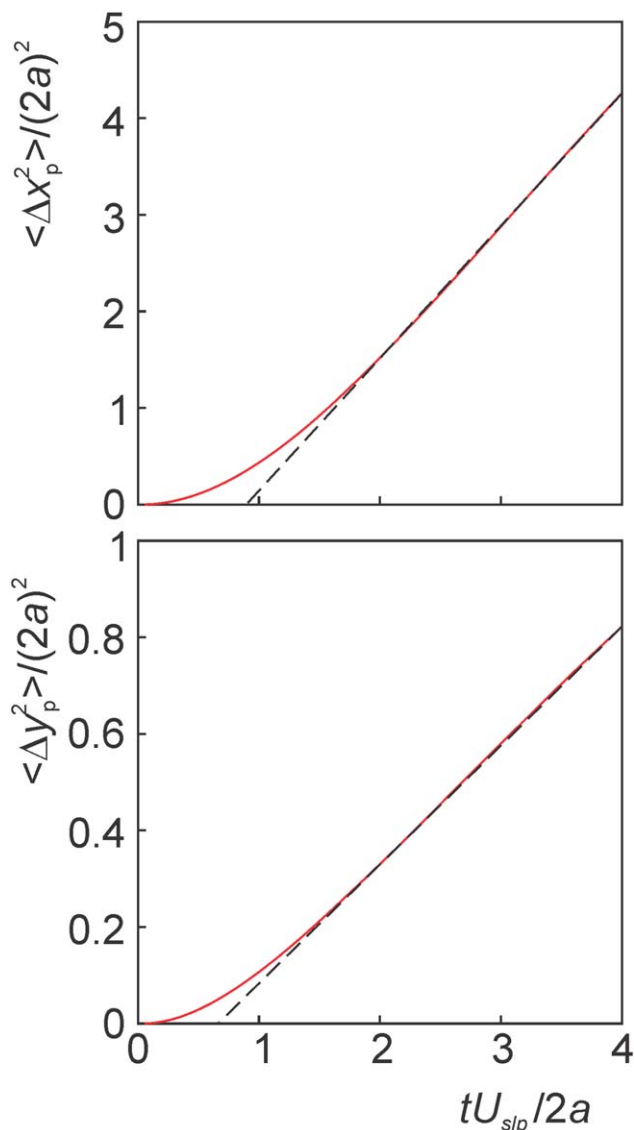


Figure 9. Red curves: time series of the mean-square displacement in vertical (x) direction and horizontal (y) direction.

The dashed lines are best fits of the approximately linear portions of the red curves. Base-case conditions. [Color figure can be viewed in the online issue, which is available at wileyonlinelibrary.com.]

same order of magnitude in vertical as well as in horizontal direction. In addition, the trends in self-diffusivity and scalar dispersion with respect to solids volume fraction and Reynolds number are quite similar. As was the case for scalar dispersion, at the high end of ϕ ($\phi = 0.5$), self-diffusivity is virtually independent of Re_∞ . Toward lower solids volume fractions, self-diffusivities increase, go through a maximum (which occurs in the range $0.3 \leq \phi \leq 0.35$) and then—at least if $Re_\infty \geq 6.0$ —decrease again. For the lowest Reynolds number ($Re_\infty = 3.3$) self-diffusivity levels off toward the low ϕ end to $\beta_{vert} \approx 8$ and $\beta_{hor} \approx 1.2$. Eventually—according to Nicolai et al.¹⁰ for $\phi \leq 0.1$ (i.e., outside the range studied in the current article)—self-diffusivity will start decreasing toward zero again.

The main difference between self-diffusivity and scalar dispersion coefficients is that the former tend to zero toward dense systems, whereas the latter do not. Extrapolation of

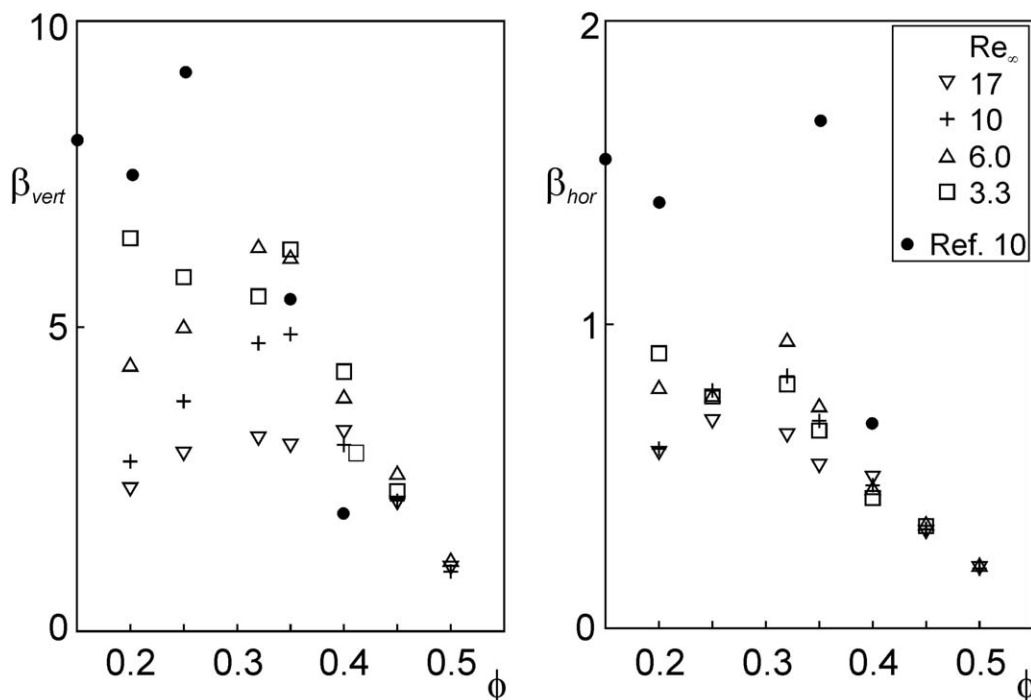


Figure 10. Dimensionless particle self-diffusivity in vertical (β_{vert} left) and horizontal direction (β_{hor} right) as a function of solids volume fraction ϕ for four different Re_∞ as indicated.

Uncertainties in β_{vert} and β_{hor} have been estimated as $\pm 10\%$. Experimental self-diffusivity data from Nicolai et al.¹⁰ (at $Re_\infty < 10^{-3}$) have been included for reference.

the trends in self-diffusivity for $\phi \geq 0.45$ teaches that self-diffusivities would reach zero at $\phi \approx 0.58$. With random close packing near $\phi \approx 0.62$,²² particles seemingly have hardly any space to maneuver beyond $\phi \approx 0.58$. Scalar dispersion, conversely, does not come to a halt at random close packing. For very dense systems dispersion remains finite as a result of liquid being convected through an (almost) packed bed. In addition to average motion, the tortuous path the liquid goes brings about dispersion (random motion). This then would be the main scalar transport mechanism at high solids volume fractions.

In our previous work on scalar mixing by moving particles,⁷ the dominant mechanism for scalar spreading was particles carrying scalar with them while moving through the liquid (we call this Mechanism-1; in short M1). Earlier we identified dispersion as a result of liquid flowing through the tortuous spaces in between the particles (packed-bed-type dispersion) as a second mechanism for scalar spreading (M2). The presence of these two mechanisms tentatively explains the behavior of scalar dispersion for the lower solids volume fractions. For lower solids volume fractions, horizontal scalar dispersion coefficients have values comparable to self-diffusion coefficients in horizontal direction. We, therefore, hypothesize that M1 is dominant for horizontal scalar spreading: scalar spreads to the same extent as particles spread. In vertical direction, scalar dispersion is some 50% stronger than self-diffusion which makes us conclude that next to M1, M2 also contributes to scalar spreading. The enhancement of scalar spreading by M2 can be appreciated by the vertical scalar distributions in Figure 5 (left panels) that particularly show a widening of the distribution in the direction of the average liquid flow.

The trends in self-diffusivity (horizontal as well as vertical) for the lower Re_∞ bear resemblance with the experimental

results in Ref. 10 (their Figure 11; note that some of the data from Ref. 10 have been included in our Figure 10). The experimental data were obtained under creeping flow conditions (particle-based Reynolds numbers $< 10^{-3}$). As witnessed from Figure 10, an increase in Re_∞ reduces (strongly for $\phi < 0.4$) the self-diffusivities. This is understood by the argument pointed out by Yin and Koch¹⁴ that lower Reynolds numbers imply longer range interactions and therefore stronger diffusivity.³⁹ As trends in scalar dispersion and self-diffusivity are similar, higher Reynolds numbers thus imply lower scalar dispersion coefficients; an effect that gets stronger towards lower ϕ .

For the base-case ($\phi=0.40$ and $Re_\infty=10.4$), effects of domain size on self-diffusivities have been investigated. Based on, for example, results for $\phi=0.20$ in Ref. 14, such effects are deemed significant. Results for taller and wider (compared to the default size) domains are summarized in Table 1. They show a systematic increase of self-diffusivities with increasing size of the domain in vertical (x) as well as horizontal direction (y and z). While the differences are almost within the accuracy margins (estimated at 10%), domain size issues need to be investigated further. We plan to do so in future work.

Summary and Conclusions

Particle-resolved simulations of solid-liquid fluidization have been performed with an emphasis on convection and diffusion of a passive scalar dissolved in the liquid. The spreading of the scalar through the liquid phase is deemed relevant for the mass transfer characteristics of this multiphase system. It has been quantified by a dispersion coefficient and we investigated how this coefficient behaved as a function of the solids volume fraction (ϕ), and the Reynolds number based on the single-particle, terminal settling velocity (Re_∞).

Table 1. Self-Diffusivities for the Base-Case, Effect of Domain Size

$n_x \times n_y \times n_z$	$48 \times 24 \times 24a^3$ (default)	$72 \times 24 \times 24a^3$	$48 \times 36 \times 36a^3$
β_{vert}	3.27	3.55	3.67
β_{hor}	0.469	0.498	0.490

Scalar spreading in the vertical direction is one order of magnitude stronger than in the horizontal directions. Vertical as well as horizontal scalar dispersion coefficients are of the same order of magnitude as the respective particle self-diffusion coefficients. This lends credit to a model that identifies particle migration as an important source for scalar spreading. Where, however, self-diffusion comes to a halt when approaching random close packing, scalar dispersion is clearly nonzero in such situations. Scalar is then being transported and dispersed in ways similar as in packed beds.

The way scalar dispersion depends on Re_∞ is consistent with what has been observed (in this article and in the literature¹⁴) for self-diffusion: a reduction of dispersion at increased Reynolds numbers as a result of shorter-range hydrodynamic interactions between spheres.

An important issue to be addressed is how the results on scalar dispersion coefficients and self-diffusivity depend on domain size and (related) the presence of bounding walls. In terms of average velocities and hindered settling behavior, it was shown that the domains are sufficiently large for the results to be independent of size. For self-diffusivity, however, systematic effects regarding domain size were observed. These effects qualitatively agree with results from the literature,^{13,14} where it needs to be borne in mind that the solids volume fractions in this study are generally higher than what has been reported previously.

Literature Cited

1. Di Felice R. Hydrodynamics of liquid fluidisation. *Chem Eng Sci.* 1995;50:1213–1245.
2. Epstein N. Applications of liquid–solid fluidization. *Int J Chem Reactor Eng.* 2003;1:R1–16.
3. Garside J, Gaska G, Mullin JW. Crystal growth rate studies with potassium sulphate in a fluidized bed crystallizer. *J Cryst Growth.* 1972;13/14:510–516.
4. Grünewald M, Schmidt-Traub H. Adsorption in multistage fluidized bed column. *Chem Eng Technol.* 1999;22:206–209.
5. Nikov I, Karamanev D. Liquid–solid mass transfer in inverse fluidized bed. *AIChE J.* 1991;37:781–784.
6. Phillips VR, Epstein N. Growth of nickel sulfate in a laboratory-scale fluidized-bed crystallizer. *AIChE J.* 1974;20:678–687.
7. Derksen JJ. Scalar mixing by granular particles. *AIChE J.* 2008;54:1741–1747.
8. Guazzelli É, Hinch J. Fluctuations and instability in sedimentation. *Annu Rev Fluid Mech.* 2011;43:97–116.
9. Snabre P, Pouligny B, Metayer C, Nadal F. Size segregation and particle velocity fluctuations in settling concentrated suspensions. *Rheol Acta.* 2009;48:855–870.
10. Nicolai H, Herzhaft B, Hinch EJ, Oger L, Guazzelli E. Particle velocity fluctuations and hydrodynamic self-diffusion of sedimenting non-Brownian spheres. *Phys Fluids.* 1995;7:12–23.
11. Koch DL. Hydrodynamic diffusion in dilute suspensions at moderate Reynolds numbers. *Phys Fluids A.* 1993;5:1141–1155.
12. Derksen JJ. Simulations of hindered settling of flocculating spherical particles. *Int J Multiphase Flow.* 2014;58:127–138.
13. Koch DL. Hydrodynamic diffusion in a suspension of sedimenting point particles with periodic boundary conditions. *Phys Fluids.* 1994;6:2894–2900.
14. Yin X, Koch DL. Velocity fluctuations and hydrodynamic diffusion in finite-Reynolds-number sedimenting suspensions. *Phys Fluids.* 2008;20:043305–1–8.

15. Ladd AJC. Hydrodynamic screening in sedimenting suspensions of non-Brownian spheres. *Phys Rev Lett.* 1996;76:1392–1395.
16. Nguyen N-Q, Ladd AJC. Sedimentation of hard-sphere suspensions at low Reynolds number. *J Fluid Mech.* 2005;525:73–104.
17. Sungkorn R, Derksen JJ. Simulations of dilute sedimenting suspensions at finite-particle Reynolds numbers. *Phys Fluids.* 2012;24:123303–1–23.
18. Chen S, Doolen GD. Lattice Boltzmann method for fluid flows. *Annu Rev Fluid Mech.* 1989;30:329–364.
19. Succi S. *The lattice Boltzmann equation for fluid dynamics and beyond.* Oxford: Clarendon Press; 2001.
20. Van Wachem BGM, Schouten JC, Van den Bleek CM, Krishna R, Sinclair JL. Comparative analysis of CFD models of dense gas–solid systems. *AIChE J.* 2001;47:1035–1051.
21. Hoomans BPB, Kuipers JAM, Briels WJ, Van Swaaij WPM. Discrete particle simulation of bubble and slug formation in a two-dimensional gas-fluidized bed: A hard-sphere approach. *Chem Eng Sci.* 1996;51:99–118.
22. Derksen JJ, Sundaresan S. Direct numerical simulations of dense suspensions: wave instabilities in liquid-fluidized beds. *J Fluid Mech.* 2007;587:303–336.
23. Schiller L, Naumann A. Über die grundlegenden Berechnungen bei der Schwerkraftaufbereitung. *Ver Deut Ing Z.* 1933;77:318–320.
24. Somers JA. Direct simulation of fluid flow with cellular automata and the lattice-Boltzmann equation. *Appl Sci Res.* 1993;51:127–133.
25. Goldstein D, Handler R, Sirovich L. Modeling a no-slip flow boundary with an external force field. *J Comput Phys.* 1993;105:354–366.
26. Ten Cate A, Nieuwstad CH, Derksen JJ, Van den Akker HEA. PIV experiments and lattice-Boltzmann simulations on a single sphere settling under gravity. *Phys Fluids.* 2002;14:4012–4025.
27. Ladd AJC. Numerical simulations of particle suspensions via a discretized Boltzmann equation. Part I: Theoretical Foundation. *J Fluid Mech.* 1994;271:285–309.
28. Sangani AS, Acrivos A. Slow flow through a periodic array of spheres. *Int J Multiphase Flow.* 1982;8:343–360.
29. Hasimoto H. On the periodic fundamental solutions of the Stokes equations and their application to viscous flow past a cubic array of spheres. *J Fluid Mech.* 1959;5:317–328.
30. Derksen JJ. Drag on random assemblies of spheres in shear-thinning and thixotropic liquids. *Phys Fluids.* 2009;083302-1-9.
31. Nguyen N-Q, Ladd AJC. Lubrication corrections for lattice-Boltzmann simulations of particle suspensions. *Phys Rev E.* 2002;66:046708-1-12.
32. Yamamoto Y, Potthoff M, Tanaka T, Kajishima T, Tsuji Y. Large-eddy simulation of turbulent gas-particle flow in a vertical channel: Effect of considering inter-particle collisions. *J Fluid Mech.* 2001;442:303–334.
33. Harten A. High resolution schemes for hyperbolic conservation laws. *J Comput Phys.* 1983;49:357–364.
34. Sweby PK. High resolution schemes using flux limiters for hyperbolic conservation laws. *SIAM J Numer Anal.* 1984;21:995–1011.
35. Hartmann H, Derksen JJ, Van den Akker HEA. Mixing times in a turbulent stirred tank by means of LES. *AIChE J.* 2006;52:3696–3706.
36. Richardson JF, Zaki WN. The sedimentation of a suspension of uniform spheres under conditions of viscous flow. *Chem Eng Sci.* 1954;8:65–73.
37. Di Felice R. The sedimentation velocity of dilute suspensions of nearly monosized spheres. *Int J Multiphase Flow.* 1999;25:559–574.
38. Gupta AK, Nguyen TT, Sanqui JAT. Characterization of the skew-normal distribution. *Ann Inst Stat Math.* 2004;56:351–360.
39. Climent E, Maxey MR. Numerical simulations of random suspensions at finite Reynolds numbers. *Int J Multiphase Flow.* 2003;29:579–601.

Manuscript received Nov. 27, 2013, and revision received Jan. 2, 2014.